tvst

DOI: 10.1167/tvst.5.3.5

Article

Spatial and Spectral Characterization of Human Retinal Pigment Epithelium Fluorophore Families by Ex Vivo Hyperspectral Autofluorescence Imaging

Tal Ben Ami[1] ✉, Yuehong Tong[1], Alauddin Bhuiyan[1], Carrie Huisingh[2], Zsolt Ablonczy[3], Thomas Ach[4], Christine A. Curcio[2], and R. Theodore Smith[1]

[1] Department of Ophthalmology, New York University School of Medicine, New York, New York, USA
[2] Department of Ophthalmology, University of Alabama at Birmingham, Birmingham, Alabama, USA
[3] Department of Ophthalmology, Medical University of South Carolina, Charleston, South Carolina, USA
[4] Department of Ophthalmology, University Hospital of Würzburg, Würzburg, Germany

Correspondence: Tal Ben Ami, Department of Ophthalmology, New York University School of Medicine, New York, New York, USA. e-mail: tbenami@gmail.com

Received: 6 October 2015
Accepted: 28 March 2016
Published: 17 May 2016

Keywords: hyperspectral imaging; retinal pigment epithelium; lipofuscin; autofluorescence imaging; bisretinoids

Citation: Ben Ami T, Tong Y, Bhuiyan A, et al. Spatial and spectral characterization of human retinal pigment epithelium fluorophore families by ex vivo hyperspectral autofluorescence imaging. Trans Vis Sci Tech. 2016;5(3):5, doi:10.1167/tvst.5.3.5

Purpose: Discovery of candidate spectra for abundant fluorophore families in human retinal pigment epithelium (RPE) by ex vivo hyperspectral imaging.

Methods: Hyperspectral autofluorescence emission images were captured between 420 and 720 nm (10-nm intervals), at two excitation bands (436–460, 480–510 nm), from three locations (fovea, perifovea, near-periphery) in 20 normal RPE/Bruch's membrane (BrM) flatmounts. Mathematical factorization extracted a BrM spectrum (S0) and abundant lipofuscin/melanolipofuscin (LF/ML) spectra of RPE origin (S1, S2, S3) from each tissue.

Results: Smooth spectra S1 to S3, with perinuclear localization consistent with LF/ML at all three retinal locations and both excitations in 14 eyes (84 datasets), were included in the analysis. The mean peak emissions of S0, S1, and S2 at λ_{ex} 436 nm were, respectively, 495 ± 14, 535 ± 17, and 576 ± 20 nm. S3 was generally trimodal, with peaks at either 580, 620, or 650 nm (peak mode, 650 nm). At λ_{ex} 480 nm, S0, S1, and S2 were red-shifted to 526 ± 9, 553 ± 10, and 588 ± 23 nm, and S3 was again trimodal (peak mode, 620 nm). S1 often split into two spectra, S1A and S1B. S3 strongly colocalized with melanin. There were no significant differences across age, sex, or retinal location.

Conclusions: There appear to be at least three families of abundant RPE fluorophores that are ubiquitous across age, retinal location, and sex in this sample of healthy eyes. Further molecular characterization by imaging mass spectrometry and localization via super-resolution microscopy should elucidate normal and abnormal RPE physiology involving fluorophores.

Translational Relevance: Our results help establish hyperspectral autofluorescence imaging of the human retinal pigment epithelium as a useful tool for investigating retinal health and disease.

Introduction

The retinal pigment epithelium (RPE) is a monolayer of cells exterior to the photoreceptors of the neurosensory retina.[1] The RPE rests on Bruch's membrane (BrM), a five-layered extracellular matrix serving both as the substrate for RPE attachment and as a vessel wall at the inner aspect of the choroidal vasculature that nourishes outer retinal cells.[2] Changes in the RPE are considered central to the initiation and progression of age-related macular degeneration (AMD), a major cause of vision loss among older persons worldwide. Among RPE's various roles, generating vitamin A derivatives required for phototransduction through a series of biochemical reactions known as the visual cycle is perhaps the one best understood.

Byproducts of the visual cycle contribute to the autofluorescence (AF) signal of lipofuscin (LF) and

melanolipofuscin (ML) granules in the lysosomal compartment of the RPE.[3] This intense signal can be clinically visualized,[4–6] and abnormalities in the clinical AF signal are strong markers for AMD and its progression.[7–9] AF attributable to LF/ML presents a single broad emission spectrum, which represents a sum of multiple constituents. Knowing the individual components of this spectrum is vital to understanding the role of the RPE in health and disease. An extensive literature on bisretinoid biochemistry describes the search for candidate RPE fluorophores.[10–15] Over 25 bisretinoid fluorophores have been extracted from LF/ML granules in the RPE, including N-retinylidene-N-retinylethanolamine (A2E),[16] generally with analytic techniques that did not preserve spatial resolution.

This study used hyperspectral imaging technology, which captures images of an object or tissue at multiple wavelengths to seek unique patterns of emission, or spectral signatures, of components within it. Detection of such signatures is widely used in many scientific fields.[17–19] We previously described a novel biomedical engineering algorithm based on nonnegative matrix factorization (NMF) for analysis of hyperspectral AF images and validated it on such ex vivo images of human RPE and BrM.[20] We demonstrated that this algorithm was capable of detecting plausible spectral signatures of abundant RPE fluorophores. The goal of the present study is to apply this image analysis tool systematically on the RPE to provide data of interest specifically to vision science, namely, a comprehensive spatial and spectral catalog of the signatures of abundant RPE fluorophore families in healthy eyes. This portfolio of information can then serve as a guide for further research with techniques that are capable of precise molecular identification of the compounds themselves, such as imaging mass spectrometry (IMS); spatial localization of the enclosing organelles, such as structured illumination microscopy[21]; and eventual extension to tissues from eyes with retinal disease. With spectra linked to specific compounds, hyperspectral imaging should achieve its full potential of spectral, molecular biopsy of the RPE, with potential for better understanding of AMD pathophysiology.

Methods

Eyes and Tissues

Twenty-μm thin flatmounts of human RPE attached to BrM (RPE/BrM) from 20 eyes lacking detectable retinal pathology, from 20 human donors, were prepared by removing the choroid and neurosensory retina, as previously described.[22] These normal specimens were part of a research repository collected from the Alabama Eye Bank (1995–2009) and were used for the study of AF and RPE cell number with age.[22,23] The ages of donors analyzed were thus dictated by the experimental design of our prior study (2 groups, >80 years and ≤51 years).

Image Acquisition

In each flatmount, three tissue areas were imaged and analyzed at fixed distances relative to the fovea: fovea center, perifovea (2-mm superior), and near-periphery (10- to 12-mm superior). The RPE in each of these locations relates to distinctive photoreceptor populations in the overlying retina: cones only, highest rod density, and highest rod/cone ratio, respectively.[24]

Microscopy was performed using a Zeiss Axio Imager A2 microscope equipped with a ×40 oil objective (numerical aperture = 0.75; Carl Zeiss, Jena, Germany) and two filter cubes (436/460 and 480/510 nm band pass excitation/long pass emission; Chroma Technology Corp., Bellows Falls, VT) and connected to an external mercury arc light source (X-Cite 120Q; Lumen Dynamics Group, Inc., Mississauga, Ontario, Canada).

We refer to the two excitation band wavelengths as λ_{ex} 436 and λ_{ex} 480 nm. At each of the three locations for each of the 20 eyes, a hyperspectral data cube from RPE and BrM was acquired at each of these wavelengths using a hyperspectral camera (Nuance FX, Nuance 3.0.1.2 software; Caliper Life Sciences, Waltham, MA), for a total of 120 tissue datasets. Upon excitation with λ_{ex} 436 and λ_{ex} 480 nm, emission spectra were captured between 420 and 720 nm and between 510 and 720 nm, respectively, at 10-nm intervals. Data were recalibrated with respect to the camera's spectral sensitivity, which is nearly linear from 450 to 700 nm.

Extraction of Fluorophore Spectra and Tissue Localizations

Custom MATLAB-based programs (MATLAB, release 2013a; MathWorks, Inc., Natick, MA) recovered the abundant spectra. The two hyperspectral emission data cubes, one for each excitation, were explored using NMF, an advanced mathematical tool which we extended to nonnegative tensor factorization (NTF), described below, for simultaneous decomposition of the two coregis-

tered hyperspectral data cubes. Briefly, the algorithm is initialized by the user, who samples the raw spectra of BrM and RPE from each data cube. The rest of the process is fully automated, so that data is acquired in an unbiased manner applied uniformly to each RPE/BrM tissue hyperspectral dataset. Next, a 4-Gaussian mixture model is fit to the RPE spectrum, and NMF analysis is initialized with the 4 Gaussians and the BrM spectrum. Finally, NMF analysis is performed simultaneously on the two excitation datasets by NTF, in which the simultaneous solutions for the recovered spectra are constrained to have identical spatial abundances.[20] At this point, the paired data from the two excitation wavelengths are treated as a single dataset. The NTF process thus recovers five abundant emission spectra for each excitation wavelength and a tissue abundance image for each spectrum that describes its spatial localization. It is important to note, however, that the solutions are not constrained by any spectral or spatial characteristics, except that the paired abundance images for signal pairs from the two excitations are held identical. It is only after the algorithm has found a set of solutions that the number of abundant spectra, their spectral peaks, and their spatial localizations are recorded.

Smooth, well-defined spectra S1 to S3 and abundances consistent with LF/ML perinuclear localization were sought at all three locations (fovea, perifovea, and near-periphery) and at both excitations. Eyes were excluded, with all their hyperspectral datasets, if at least one location had spectra that was missing or uninterpretable (i.e., nearly flat or with multiple sharp peaks). The purpose of these exclusions was to avoid missing data when comparisons were made between locations in the final dataset. Three excluded tissues consisted almost entirely of bare BrM due to preparation RPE loss, and as a result, the RPE signals were low intensity and/or noisy. In three other tissues, the algorithm simply failed to recover interpretable spectra from the hyperspectral data. The excluded specimens were randomly distributed in age, sex, and retinal location. A total of 14 eyes from 14 donors were thus chosen for analysis (3 locations per eye, 2 excitation wavelengths per location, for a total of 84 hyperspectral datasets). Spectra were analyzed and compared by the location of their peaks and by their shapes (single peak versus multiple peaks). Spectral shapes were further compared in selected cases by the metric of the spectral angle distance (SAD), a geometric interpretation of correlation, which for two spectra, S and $\hat{S}$. S defined as follows:

$$\mathrm{SAD}(\hat{S}, S) = \cos^{-1}\left(\frac{S^{\mathrm{T}}\hat{S}}{\sqrt{S^{\mathrm{T}}S}\sqrt{\hat{S}^{\mathrm{T}}\hat{S}}}\right) \qquad (1)$$

where S^{T} is the transpose of S. This angle takes the value 0 if the spectra are perfectly correlated and takes the maximum value $\pi/2$ (or 90°) if the spectra are completely uncorrelated.[25]

For studying colocalization, overlaying abundance images in a suitable image manipulation program (Photoshop CC 2015; Adobe Systems, San Jose, CA) was more informative than side-by-side inspection. Further, by assigning standard colors (not the wavelengths of the emissions) to each of the overlaid signal abundances, with appropriate mixing, we false-colored the tissue to provide a visually intuitive interpretation of colocalizations and relative intensities. If one signal abundance is assigned the color green, and another red, then areas where they colocalize will appear yellow, or perhaps orange if the red signal is more abundant.

Tissue colocalizations of the abundances (spectral sources) were also calculated quantitatively in selected examples with the Pearson correlation coefficient using a custom MATLAB program. For tissues in which patches of bare BrM were present, a mask was first applied to eliminate BrM from the calculation of correlations between LF/ML spectra.

Statistical Analysis

Extracted data were analyzed with descriptive and inferential statistics using SPSS Version 22 (IBM Corp., Armonk, NY). The χ^2 test was used to compute categorical outcomes. Type I error was set at 0.05. The positions of the hyperspectral AF peaks assigned to each LF/ML spectral component were further compared between young and aged eyes at the different retinal locations using a Wilcoxon Mann-Whitney U test. "Young" was defined as less than or equal to 51 years, and "aged" was defined as greater than or equal 80 years.

Results

Subjects

The ages of the 14 donors ranged from 16 to 90 years, divided into seven young and seven aged; 29% were male, and 71% were female. Donor demographics can be found in the Table and in Supplementary Table S1.

Table. Mean Emission Maxima of the Abundant Fluorophore Signals (nm)

λ_{ex}, nm	436–480						480–510					
Signal Family	S0	S1	S1A	S1B	S2	S3	S0	S1	S1A	S1B	S2	S3
Prevalence*	38	42	17	17	38	39	29	36	18	18	39	37
Mean peak signal, nm	495	535	526	546	576	635	526	553	549	561	588	628
SD, nm	14	17	15	19	20	26	9	10	9	12	23	24
Location												
Fovea ($n = 14$)	495	537	532	564	574	629	522	555	550	566	581	622
Perifovea ($n = 14$)	494	534	525	543	579	637	526	553	550	559	593	635
Near-periphery ($n = 14$)	495	533	523	533	574	641	534	552	547	557	591	627
Sex												
Male ($n = 15$)	500	529	518	534	572	642	527	551	550	560	592	628
Female ($n = 27$)	491	538	530	552	577	631	526	555	549	561	587	627
Age												
$\leq$ 51 years ($n = 21$)	495	536	523	549	575	636	526	553	547	562	594	624
$\geq$ 80 years ($n = 21$)	494	533	530	544	576	635	526	554	553	559	584	631

* Prevalence of recovered spectra from each family from a total of 42 locations in 14 tissues.

Major Spectral Emissions

The five individual recovered spectra in the 436-nm set were labeled and color coded as follows: in the first pass, the three most abundant LF/ML signals in peak wavelength order were assigned to S1 (green), S2 (blue), and S3 (red). S0 (gray) was assigned to the spectrum localizing to BrM. However, it was apparent that in many, but not all, cases there were two signals in the 500- to 550-nm range, at which S1 typically appeared. We chose to identify these as S1A and S1B (green and azure, respectively); the next signal was then S2 (blue), and so on. S1A and S1B appeared to be the splitting of S1 into two signals, suggesting two families with similar emissions. In all, 19/42 imaging locations showed a split S1 at one wavelength or both, with 16 showing split signals at both wavelengths. When S1 was not split into S1A and S1B, then in addition to S0 (BrM) and S1, S2, and S3 (all LF/ML), a fifth, variable spectrum was recovered in some cases. It was labeled SX and assigned a new color (magenta); the abundance for SX, however, was clearly BrM and/or LF/ML in all cases. The signals at 480 nm were then tabulated in peak wavelength order to correspond with their counterparts at 436 nm, except as noted below. An example in which all signals are evident at each excitation wavelength is in Figure 1A.

Spectral Signatures by Peak Emission

The distribution of recovered spectra from all 42 tissue locations is detailed in Table. The peak emissions of the BrM (S0) and S1A, S1B, S2, and S3 signals at λ_{ex} 436 nm were 495 ± 14, 526 ± 15, 546 ± 19, 576 ± 20, and 635 ± 26 nm, respectively. At λ_{ex} 480 nm, S0, S1A, S1B, and S2 were red-shifted (relative to their λ_{ex} 436-nm counterparts) to 526 ± 9, 549 ± 9, 561 ± 12, and 588 ± 23 nm, respectively, and S3 was slightly blue-shifted to 628 ± 24 nm, although this last peak was more variable at both excitations due to the trimodal nature of S3 (see Discussion). In those tissues where S1 was split, S1A and S1B were added together to give an approximate version of S1, and the peak of this recombined S1 was tabulated to compare with the peaks of those S1 that were not split. A nearly uniform finding in each of the S1, S1A, S1B, and S2 signals, at both excitation wavelengths, was a secondary peak or shoulder at 601 ± 4 nm (Fig. 1A, black arrows). Because of the ubiquity of this finding, we recorded it as a separate phenomenon.

Primary and secondary peaks for all spectra are presented in Supplementary Table S2.

Spectral Signatures by Shape

The shape of the spectrum is as important a descriptor as the peak, especially for complex molecular species, or families of such species. The longest wavelength spectrum S3 tended to be trimodal, with peaks and/or shoulders, P1, P2, and P3, near 580, 620, and 650 nm. The actual peak of S3 (i.e., the highest peak of P1–P3) at λ_{ex} 436 nm was most commonly at 650 nm, appearing in 21/38 tissue

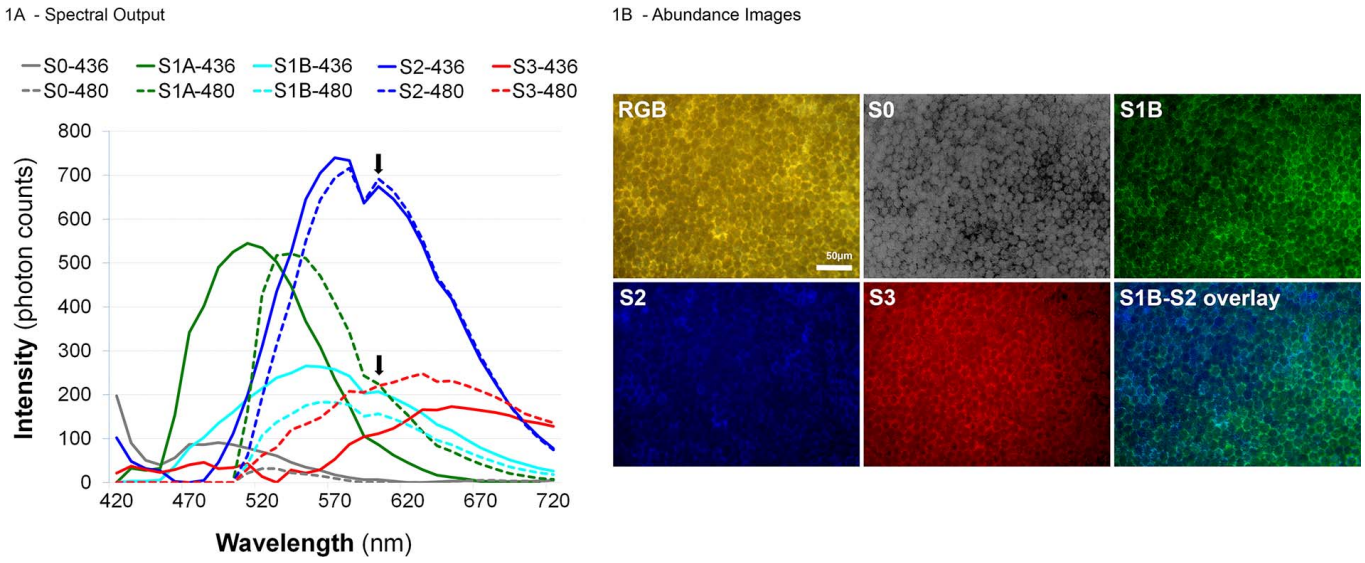

Figure 1. (A) NMF spectral output (16-year-old male donor, fovea), with trimodal S3 and secondary peaks/shoulders in S1A, S1B, and S2. All 10 representative spectra are present. The five *solid lines* are emission spectra at λ_{ex} 436 nm; the 5 *dashed lines* are emission spectra at λ_{ex} 480 nm. S0 is BrM. All others are LF/ML spectra (see abundances, [B]). Note that S3 at λ_{ex} 436 nm has a peak near 650 nm but also has shoulders near 580 and 630 nm (*trimodal shape* typical of S3). This spectrum also has a secondary peak near 475 nm, often seen in S3 at λ_{ex} 436 nm. S3 at λ_{ex} 480 nm is also trimodal in shape; here the peak is near 630 nm, with shoulders near 580 and 650 nm. Despite the fact that the two S3 spectra have different peaks, the similarities in shape and the alignment of the three modes are clear; the spectral angle between them (Equation 1) is 19°. The S2 spectra are extraordinarily similar and are separated by a spectral angle of only 6°. Likewise, the S1A spectra track each other closely from approximately 540 nm on; the spectral angle is 11°. By contrast, the S2 and S3 spectra at λ_{ex} 436 nm are separated by 44°. Also note the secondary peaks or shoulders in S1A, S1B, and S2 at approximately 600 nm at both excitations (*black arrows*). These peaks or shoulders are virtually ubiquitous in these three spectra; a separate spectrum with a single peak near 600 nm is rarely recovered. (B) Abundance images for spectra recovered from tissue in (A); localization of BrM signal; differential localization of fluorophore families. The abundance image for S1A (not shown) is rather similar to that for S1B (Pearson correlation coefficient, $r = +0.78$). Note that the abundance for S0, which is from BrM, "shines through" the RPE cells, except where it is blocked by abundant LF. Although the abundances of all the LF/ML fluorophores are quite similar on side-by-side inspection, the overlay of S2 and S3 clearly demonstrates that S2 is more abundant in some regions, and S3 is more abundant in others. Indeed, comparison of the overlay with the original RGB image reveals that S2 predominates where the classic yellow of lipofuscin AF is seen, and S3 predominates where melanin is abundant, suggesting a differential localization of S3 to ML, confirmed by a moderate correlation ($r = +0.74$). S2 has a patchier distribution than S1B, which is more homogeneous, but these two LF spectra are also moderately colocalized ($r = +0.76$).

locations in which S3 was found. At λ_{ex} 480 nm, S3 was again trimodal, with peak mode at 620 nm in 19/36 tissue locations in which S3 was found. Because the actual peak varied, the overall mean peak of S3 was less informative, but the shapes of the S3 spectra were recognizably the same. Thus, the SAD was particularly useful for demonstrating similarities in recovered spectra that should be assigned to S3 and distinguishing them from other spectra (Fig. 1A). Details of the three modes of S3 are tabulated in Supplementary Table S3. For S3 at λ_{ex} 436 nm only, an additional peak often appeared (33/42 tissues) in the blue range at approximately 475 nm, completely separate from the main S3 spectrum in the orange-red range.

Subcellular Localization of Fluorophore Spectral Sources

Of equal importance to the peaks and shapes of the spectra recovered are the tissue sources of those spectra, shown as abundance images. In particular, appropriate perinuclear tissue localizations of the LF/ML spectra were documented in all cases.[20] To better correlate the spectral abundances with the anatomic features (e.g., nuclei and melanosomes), a combined spectral AF image from all channels was used (Fig. 1B, RGB panel). S3 localized more specifically to melanin in all tissues examined. S1, S1A, S1B, and S2 generally showed a more homogeneous localization throughout the perinuclear region.

The tissue abundances provided by the NMF

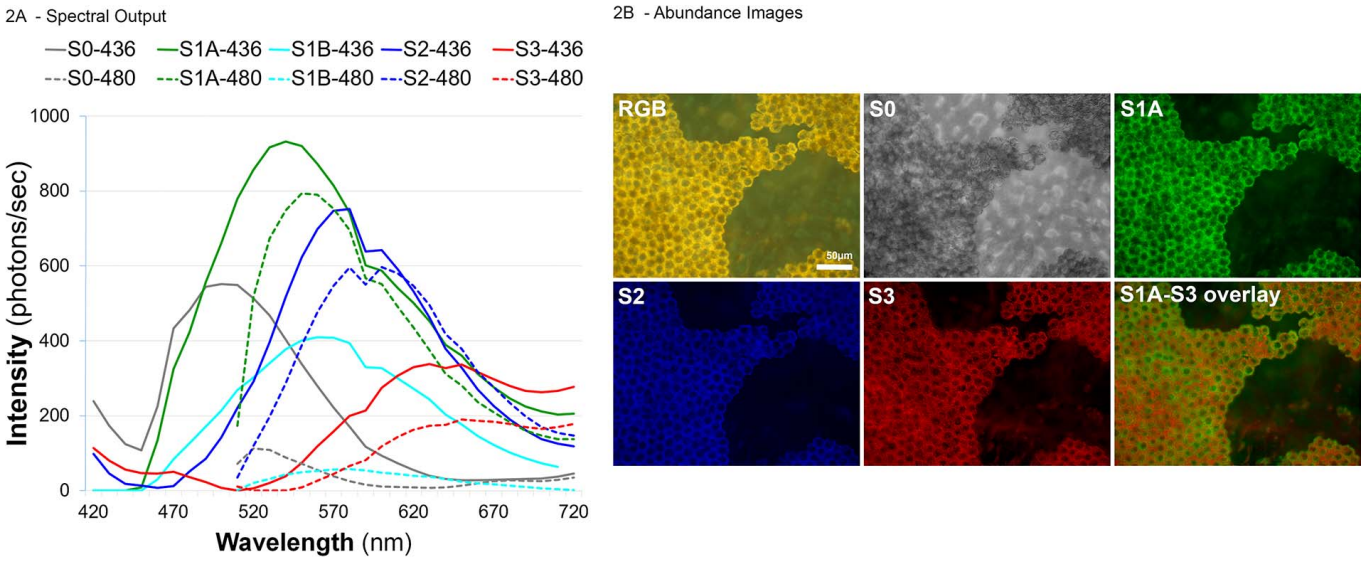

Figure 2. (A) NMF spectral output (36-year-old male, perifovea); splitting of S1 into S1A and S1B. In this example, spectrum S1 splits into two spectra, S1A and S1B. S0 is BrM. All others are LF/ML spectra (see abundances, [B]). S2 has its peak around 600 nm, with a shoulder at 575 nm, rather than its usual peak at 575 nm. S3 at λ_{ex} 436 nm is *solid red*. Notice the extra peak at 475 nm commonly seen in this signal (compare Fig. 1A). (B) Abundance images for spectra recovered in (A); differential tissue localizations. In this tissue with bare BrM, S0 strongly localizes to BrM, revealing the origin of this signature, and also "shines through" the RPE nuclei. The abundances of the LF/ML spectra S1A, S2, and S3 are all similar and track the lipofuscin abundance in the RGB panel, with minimal localization to BrM. Overlay S1A and S3. The differential localization of S1A and S3, however, reveals that their abundances are not identical. In fact, the areas where S3 predominates correspond well with the brown material in the RGB image (i.e., granules containing melanin, consistent with the hypothesis that S3 is the spectrum of ML).

technique unambiguously assigned a spectral signature to either BrM or LF/ML. In most cases, there was an area of bare BrM that made assignment to BrM obvious. In samples without any bare BrM, the typical short wavelength signature had abundance coincident with the RPE nuclei, consistent with presence of BrM beneath the RPE and relative lack of RPE fluorophore through the vertical light path through the nucleus. We refer to this phenomenon as "nuclear shine-through." However, in 16/42 tissue locations, the shortest wavelength spectrum S0 localized to both BrM and LF/ML compartments, and it was completely absent in 6/42. That one spectrum could localize to both RPE and BrM may signify that a certain fluorophore is indeed abundant in both, or it might simply be a limitation of the method in spectral resolution. Conversely, in some other tissues with large areas of bare BrM, two distinct BrM spectra were recovered, S0 and SX (Fig. 3B). This is not surprising, because we have already shown hyperspectral retrieval of multiple AF spectra from pure BrM.[20] The remaining three spectra in these cases were abundant LF/ML spectra S1, S2, and S3.

Tissue Colocalization of Fluorophore Spectral Sources

Colocalization of S1, S1A, S1B, and S2 was moderately strong when the abundances were overlaid via color mixing. This was confirmed by the Pearson correlation coefficients, as demonstrated in Figure 3B. A high correlation between S1A and S1B ($r \geq 0.70$) was found in all cases when S1 splitting occurred. Generally, correlations of either S1, S1A, or S1B with S2 were also moderately strong, with similar ranges. In Figure 3B, S3 localized to melanin on the abundance overlay, as opposed to S1 and S2, which localized to LF, with resulting low correlations between S3 and S1 or S2. This was confirmed by a low Pearson correlation between S2 and S3 ($r = -0.11$). In general, the correlations of either S1, S1A, S1B, or S2 with S3 varied widely with the amount of visible melanin, from essentially uncorrelated (in tissues with abundant visible melanin) to moderately correlated ($r \geq 0.70$, where melanin was less abundant) (Fig. 1B).

Subgroup Analysis

Subgroup analysis of the λ_{ex} 436-nm dataset for location (fovea, perifovea, and near-periphery), age

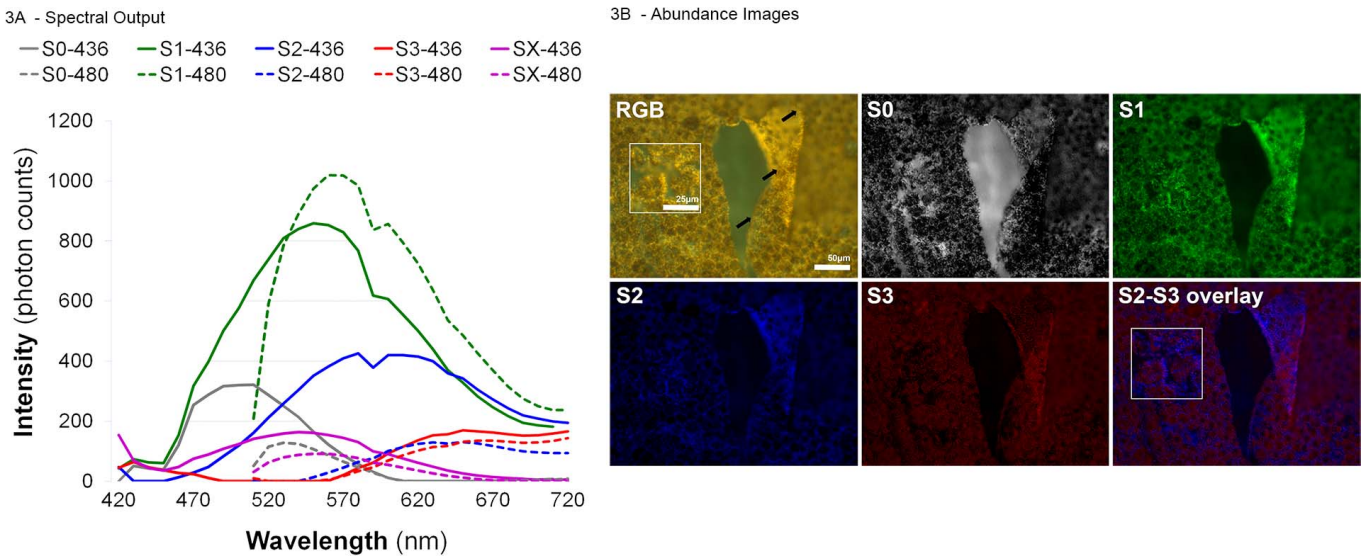

Figure 3. (A) NMF spectral output (36-year-old male, near-periphery). S0 is the usual BrM spectrum; SX is a second BrM spectrum. S1, S2, and S3 are the basic LF/ML spectra. (B) Abundance images for spectra recovered from tissue in (A); localization of S3 to ML; dual BrM spectra. BrM is exposed where a flap (*black arrows*) was everted in the RPE monolayer. S0 localizes to BrM, with variegation corresponding to the intercapillary pillars and with no "nuclear shine-through" as commonly seen in other BrM signals. However, the abundance of the longer wavelength SX also localizes to BrM, but in a completely homogeneous distribution, and displays prominent nuclear shine-through. Indeed, for the BrM signals, there is a slight decorrelation (Pearson correlation coefficient, $r = -0.11$). The underside of the flap is brighter than the rest of the RPE because most melanin is apical, increasing absorption of the AF signal. The abundances of LF/ML spectra S1 and S2 are quite similar ($r = +0.76$; S1 not shown). Note the differences between the S2 and S3 abundances, as demonstrated in the overlay panel and insert: S2 is abundant in areas corresponding with LF granules, while S3 localizes to areas rich in ML granules. Compare overlay inset with inset in RGB panel. S2 and S3 are actually uncorrelated ($r = -0.19$). The correlation of S1 and S3 is small ($r = +0.04$). As would be expected, the correlations of the BrM spectra with the LF/ML spectra range from uncorrelated (S3 and SX, $r = +0.01$) to anticorrelated (S1 and SX, $r = -0.55$).

(young and aged eyes), and sex showed only one possibly significant difference in spectral peaks: between age groups in the near-periphery for peak S3 (643 nm for young eyes, 635 nm for aged eyes, $P = 0.0351$, t-test). We further compared peak wavelength values at each excitation wavelength between young and aged eyes at each specific location using a Wilcoxon Mann-Whitney U test. Overall, the values were similar between young and aged eyes. Because results appeared similar across locations, they were combined (for more power) to compare values between young and aged eyes overall. Generalized estimating equations were used to account for the within-person correlation. Adjustment of P values for multiple comparisons was not performed. There were no significant differences between young and aged eyes overall.

Discussion

Hyperspectral imaging technology is well known in space science, satellite surveillance, and quality control and is still emerging in medical science. Hyperspectral reflectance imaging has previously been used to measure oxygen saturation levels in the retinal vasculature,[26] as well as to demonstrate dynamic oximetry in human eyes.[27] The current study extends hyperspectral technology to AF imaging of the RPE and its fluorophores.

The molecules responsible for RPE AF have received considerable attention during the last 3 decades. AF is a convenient imaging modality to follow pathological changes in a clinical setting; however, by itself, it is not molecularly specific. This is particularly true in RPE AF, where the emission spectra are broad, resulting in ambiguity in identifying individual small molecules from a family of similar molecules, particularly bisretinoid-like compounds. Here, we enhanced traditional AF imaging with hyperspectral imaging and analysis, which is a significant step toward higher specificity attainable in a clinical setting.

Herein, we build on our prior study of healthy subjects showing stability of RPE cell number and increased overall AF in older versus younger adults.[22] We applied hyperspectral AF imaging and a novel

analytic technique[20] to these same RPE/BrM flatmounts to identify at least three spectral signatures in the human RPE that appear to represent distinct families of RPE fluorophores. Spectrum S1 often resolved into two spectra, S1A and S1B, suggesting that two families were present in S1, making four in all. These recovered signatures provide consistent candidates for spectra of major fluorophore families across age, sex, and retinal location with appropriate perinuclear localizations. Overlaying the abundance images demonstrated further differential spectral localization to tissue compartments (Figs. 1B–3B, overlay panels) of potential biologic significance. More specifically, the LF/ML spectra S1 (or S1A and S1B) and S2 generally had perinuclear abundances that were similar, except for intensity, across broad regions of RPE, suggesting that, at our current level of resolution, these fluorophore families track together. Whether this is maintained at higher resolutions and at the level of individual granules remains to be determined. S3, however, almost always presented a coarsely granular appearance and, while maintaining largely a perinuclear abundance, also appeared to colocalize more with melanosomes or ML, where present (Figs. 2B, 3B), than with LF. These observations were validated by correlation coefficients of the abundance images in selected cases. This suggests, but does not prove, that S3 is the main signal from ML.

The spectral separation of signals was incomplete in some cases, with individual spectra recovered in combinations. An example is the splitting of S1 into S1A and S1B in nearly half of the cases. Furthermore, secondary peaks and shoulders at 601 nm in S1, S1A, S1B, and S2 were very consistent, but we recovered a spectrum with a single peak at 601 nm only rarely. Whether this phenomenon represents a consistent, secondary emission in the already identified spectra of the three main fluorophore families, or just inability of the current method to separate another family spectrally, is yet to be determined. Another possibility is that these ubiquitous inflections at 601 nm were of instrumental origin. We consider this unlikely, because isolated A2E on BrM imaged using the same camera provides a smooth spectrum without secondary peaks or shoulders near 600 nm (data not shown).

Strengths of this study are the relatively large number of datasets and their broad representations of age, retinal location, and sex. The excellent quality of the RPE/BrM flatmounts analyzed and the consistency of the spectral and spatial data recovered are also of great importance. Regarding consistency, a major strength is that the extracted signals were found in an unbiased manner by a published automatic algorithm applied uniformly to each RPE/BrM tissue hyperspectral dataset.

The study had several limitations. The 20 original donor eyes excluded middle-aged donors so as to analyze AF and RPE cell numbers at extremes of age in a previous study,[22] perhaps biasing our present findings. Studying a more complete range of ages would be a desirable future goal. Six of 20 original donor eyes were excluded from this study for technical reasons (preparation tissue loss or algorithm failure), perhaps also introducing bias, although the samples involved were randomly distributed in age, sex, and retinal location. Modifications of the algorithm will be tested in future work to see if these problems can be overcome. We limited our search with the NMF analysis technique itself to four abundant LF/ML signals and one BrM signal from each tissue, and data were obtained at only two excitation wavelengths. Further research could acquire more hyperspectral data from additional excitation wavelengths, allowing comparison with excitation spectra of known bisretinoids for molecular identification and simultaneous analysis by NTF for improved spectral recovery. Given the multiple comparisons, it is possible that some significant associations arose due to chance.

In conclusion, we discovered with ex vivo hyperspectral imaging of human RPE at least three, perhaps four, distinct LF/ML AF spectra, which have well-defined emission characteristics at two excitation wavelengths and which appear to be universally present in healthy eyes across age, sex, and retinal location. This strongly suggests that there are at least three corresponding abundant families of RPE fluorophores with these characteristic signatures that remain to be identified biochemically by techniques such as IMS and localized to specific granule populations by super-resolution microscopy techniques. The fluorophore families corresponding to these spectra should then account for essentially all significant normal human RPE fluorescence, because the consistent successful factorization by NMF of the original spectral AF data, by definition, has reconstructed the entire RPE emission from 42 representative tissues, with very small error.

Finally, our long-term goal is to translate these methods to human eyes in vivo, using a snapshot hyperspectral camera,[27] and provide a straightforward and noninvasive method for evaluating the RPE fluorophores. Altered and/or new fluorophores may be expected in AMD, as well as redistribution of normal fluorophores, as published[28] and preliminarily presented (Ben Ami T, et al. *IOVS*. 2015;56(7):ARVO

E-Abstract 4369; Tong Y, et al. *IOVS*. 2015;56(7):ARVO E-Abstract 3956). Thus, although the usefulness of hyperspectral imaging in AMD is as yet unproven, the success of the method presented here in normal tissues ex vivo suggests the potential of spectral, molecular biopsy of the RPE in vivo for early detection, longitudinal follow-up, and target discovery for AMD.

Acknowledgements

Supported by grants from National Eye Institute (NEI)/National Institutes of Health (NIH) R01 EY021470 and Foundation Fighting Blindness Individual Investigator Award (RTS); NEI/NIH R01 EY06109 (CC); NEI/NIH EY19065 (ZA); German Research Foundation DFG # AC265/1-1 and # AC265/2-1 (TA); Unrestricted funds from Research to Prevent Blindness (to the University of Alabama at Birmingham, New York University School of Medicine, and Medical University of South Carolina).

Disclosure: **T. Ben Ami,** None; **Y. Tong,** None; **A. Bhuiyan,** None; **C. Huisingh,** None; **Z. Ablonczy,** None; **T. Ach,** None; **C.A. Curcio,** None; **R.T. Smith,** None

References

1. Ts'o MO, Friedman E. The retinal pigment epithelium. I. Comparative histology. *Arch Ophthalmol*. 1967;78:641–649.
2. Curcio CA, Johnson M. Structure, function, and pathology of Bruch's membrane. In: Ryan SJ, Schachat AP, Wilkinson CP, Hinton DR, Sadda S, Wiedemann P, eds. Retina. London, UK: Elsevier; 2013:466–481.
3. Sparrow JR, Wu Y, Kim CY, Zhou J. Phospholipid meets all-trans-retinal: the making of RPE bisretinoids. *J Lipid Res*. 2010;51:247–261.
4. Feeney L. Lipofuscin and melanin of human retinal pigment epithelium. Fluorescence, enzyme cytochemical, and ultrastructural studies. *Invest Ophthalmol Vis Sci*. 1978;17:583–600.
5. Ng KP, Gugiu B, Renganathan K, et al. Retinal pigment epithelium lipofuscin proteomics. *Mol Cell Proteomics*. 2008;7:1397–1405.
6. Tang PH, Kono M, Koutalos Y, Ablonczy Z, Crouch RK. New insights into retinoid metabolism and cycling within the retina. *Prog Retin Eye Res*. 2013;32:48–63.
7. Delori FC, Fleckner MR, Goger DG, Weiter JJ, Dorey CK. Autofluorescence distribution associated with drusen in age-related macular degeneration. *Invest Ophthalmol Vis Sci*. 2000;41:496–504.
8. Hwang JC, Chan JW, Chang S, Smith RT. Predictive value of fundus autofluorescence for development of geographic atrophy in age-related macular degeneration. *Invest Ophthalmol Vis Sci*. 2006;47:2655–2661.
9. Rudolf M, Vogt SD, Curcio CA, et al. Histologic basis of variations in retinal pigment epithelium autofluorescence in eyes with geographic atrophy. *Ophthalmology*. 2013;120:821–828.
10. Feeney-Burns L, Berman ER, Rothman H. Lipofuscin of human retinal pigment epithelium. *Am J Ophthalmol*. 1980;90:783–791.
11. Eldred GE, Katz ML. Fluorophores of the human retinal pigment epithelium: separation and spectral characterization. *Exp Eye Res*. 1988;47:71–86.
12. Jang YP, Matsuda H, Itagaki Y, Nakanishi K, Sparrow JR. Characterization of peroxy-A2E and furan-A2E photooxidation products and detection in human and mouse retinal pigment epithelial cell lipofuscin. *J Biol Chem*. 2005;280:39732–39739.
13. Kim SR, Jang YP, Jockusch S, Fishkin NE, Turro NJ, Sparrow JR. The all-trans-retinal dimer series of lipofuscin pigments in retinal pigment epithelial cells in a recessive Stargardt disease model. *Proc Natl Acad Sci U S A*. 2007;104:19273–19278.
14. Wu Y, Fishkin NE, Pande A, Pande J, Sparrow JR. Novel lipofuscin bisretinoids prominent in human retina and in a model of recessive Stargardt disease. *J Biol Chem*. 2009;284:20155–20166.
15. Yamamoto K, Yoon KD, Ueda K, Hashimoto M, Sparrow JR. A novel bisretinoid of retina is an adduct on glycerophosphoethanolamine. *Invest Ophthalmol Vis Sci*. 2011;52:9084–9090.
16. Sparrow JR, Gregory-Roberts E, Yamamoto K, et al. The bisretinoids of retinal pigment epithelium. *Prog Retin Eye Res*. 2012;31:121–135.
17. Kanagasingam Y, Bhuiyan A, Abramoff MD, Smith RT, Goldschmidt L, Wong TY. Progress on retinal image analysis for age related macular degeneration. *Prog Retin Eye Res*. 2014;38:20–42.
18. Lu G, Fei B. Medical hyperspectral imaging: a review. *J Biomed Optics*. 2014;19:10901.
19. Gao L, Smith RT. Optical hyperspectral imaging in microscopy and spectroscopy - a review of data acquisition. *J Biophotonics*. 2015;8:441–456.

20. Smith RT, Post R, Johri A, et al. Simultaneous decomposition of multiple hyperspectral data sets: signal recovery of unknown fluorophores in the retinal pigment epithelium. *Biomed Optics Express*. 2014;5:4171–4185.
21. Ach T, Best G, Rossberger S, Heintzmann R, Cremer C, Dithmar S. Autofluorescence imaging of human RPE cell granules using structured illumination microscopy. *Br J Ophthalmol*. 2012; 96:1141–1144.
22. Ach T, Huisingh C, McGwin G Jr, et al. Quantitative autofluorescence and cell density maps of the human retinal pigment epithelium. *Invest Ophthalmol Vis Sci*. 2014;55:4832–4841.
23. Ach T, Tolstik E, Messinger JD, Zarubina AV, Heintzmann R, Curcio CA. Lipofuscin redistribution and loss accompanied by cytoskeletal stress in retinal pigment epithelium of eyes with age-related macular degeneration. *Invest Ophthalmol Vis Sci*. 2015;56:3242–3252.
24. Curcio CA, Sloan KR, Kalina RE, Hendrickson AE. Human photoreceptor topography. *J Comp Neurol*. 1990;292:497–523.
25. van deer Meer F. The effectiveness of spectral similarity measures for the analysis of hyperspectral imagery. *International Journal of Applied Earth Observation and Geoinformation*. 2006;8:3–17.
26. Kashani AH, Lopez Jaime GR, Saati S, Martin G, Varma R, Humayun MS. Noninvasive assessment of retinal vascular oxygen content among normal and diabetic human subjects: a study using hyperspectral computed tomographic imaging spectroscopy. *Retina*. 2014;34:1854–1860.
27. Gao L, Smith RT, Tkaczyk TS. Snapshot hyperspectral retinal camera with the Image Mapping Spectrometer (IMS). *Biomed Opt Express*. 2012;3: 48–54.
28. Ablonczy Z, Smith N, Anderson DM, et al. The utilization of fluorescence to identify the components of lipofuscin by imaging mass spectrometry. *Proteomics*. 2014;14:936–944.